Delft University of Technology

Integrated Aeroelastic Measurements of the Periodic Gust Response of a Highly Flexible WIng

Mertens, C.; Costa Fernandez, J.L.; Sodja, J.; Sciacchitano, A.; van Oudheusden, B.W.

Publication date
2022

Document Version
Final published version

Published in
International Forum on Aeroelasticity and Structural Dynamics

Citation (APA)
Mertens, C., Costa Fernandez, J. L., Sodja, J., Sciacchitano, A., & van Oudheusden, B. W. (2022). Integrated Aeroelastic Measurements of the Periodic Gust Response of a Highly Flexible WIng. In *International Forum on Aeroelasticity and Structural Dynamics* Article IFASD 2022-132

Important note
To cite this publication, please use the final published version (if applicable).
Please check the document version above.

Copyright
Other than for strictly personal use, it is not permitted to download, forward or distribute the text or part of it, without the consent of the author(s) and/or copyright holder(s), unless the work is under an open content license such as Creative Commons.

Takedown policy
Please contact us and provide details if you believe this document breaches copyrights.
We will remove access to the work immediately and investigate your claim.

This work is downloaded from Delft University of Technology.
For technical reasons the number of authors shown on this cover page is limited to a maximum of 10.

International Forum on Aeroelasticity and Structural Dynamics
IFASD 2022
13-17 June 2022, Madrid, Spain

INTEGRATED AEROELASTIC MEASUREMENTS OF THE PERIODIC GUST RESPONSE OF A HIGHLY FLEXIBLE WING

Christoph Mertens[1], José L. Costa Fernández[1], Jurij Sodja[1], Andrea Sciacchitano[1], Bas W. van Oudheusden[1]

[1]Delft University of Technology
Kluyverweg 1, 2629HS Delft, The Netherlands
C.Mertens@tudelft.nl

Keywords: Pazy wing, wind tunnel testing, gust generator, Lagrangian particle tracking, unsteady aerodynamics, large deflections

Abstract: The aeroelastic response of a highly flexible wing to periodic gust excitation is determined experimentally. The integrated optical measurement approach that is applied provides combined measurements of the structural response of the wing and the unsteady flow field around it. The aeroelastic loads acting on the wing are derived from these measurements using physical models and validated against force balance measurements. It is observed that both structural and aerodynamic responses to a periodic gust excitation of a given amplitude depend strongly on the frequency of the gust. The obtained data set of results provides a complete description of the aeroelastic response that is suited as a reference for the development of aeroelastic simulation models.

1 INTRODUCTION

A current trend in aviation is towards the use of more flexible lifting structures, mainly driven by the desire to improve efficiency by saving structural weight. As a consequence, larger structural deformations are observed and aeroelastic effects become more relevant. For very flexible wings, the structural deformation can become so large as to introduce nonlinear aerodynamic and structural effects that violate the assumptions employed in linear aeroelastic prediction models [1]. These effects are amplified in the case of a gust inflow condition, which leads to increased loads on the wing compared to steady inflow. While the development of novel improved aeroelastic prediction methods that account for these nonlinear effects is currently ongoing [2–4], an experimental benchmark of a highly flexible wing, known as the Pazy wing, has recently been introduced to support these activities with experimental reference data [5]. This wing has been shown to sustain very large deformations, with wingtip displacements of up to 50% of the span.

The production of reference data from aeroelastic wind tunnel experiments is challenging due to the interaction of the three forces comprising Collar's triangle (aerodynamic, inertial, elastic) [6], which would ideally be all quantified based on the experimental measurement data. A variety of diagnostics exists to measure the individual physical quantities that allow the determination of each of the forces locally (e.g., pressure transducers, accelerometers, strain gauges) or in an integral sense by mounting the wing at the root to load cells or a force balance, but their coordinated use results in complex and expensive experimental setups. Additionally, installed sensors are invasive to the experimental model, thus modifying its mass and stiffness

distributions, as well as typically achieving only a relatively low spatial resolution due to space limitations inside the model. As a result, the experimental reference data from aeroelastic wind tunnel measurements on flexible wings that are available in the published literature are usually limited to only a few parameters, such as the wingtip deflection or the frequency of the dynamic motion [7].

Optical measurement techniques, such as photogrammetry [8] for measuring the structural response and particle image or tracking velocimetry (PIV/PTV, [9]) for aerodynamic measurements, permit non-intrusive field measurements and hence overcome many of the limitations associated with the use of installed sensors. On the other hand, the drawback of these non-intrusive techniques is that the determination of the aeroelastic forces from the measured quantities, such as structural displacements or flow velocity, is not straightforward. This topic has therefore been subject to considerable research efforts in recent years [10–12]. Despite this additional effort, the advantages of optical measurement techniques are prevailing and several recent studies have employed optical measurement techniques for characterizing fluid-structure interactions in wind tunnel experiments [13–15]. A common issue in these studies is tackling the complication of the experimental setup and the data processing that arises from the coordinated use of different optical measurement systems or techniques to obtain the structural and flow measurements. A measurement approach that does not suffer from this limitation is Lagrangian Particle Tracking (LPT). It was recently shown that LPT, implemented via the Shake-The-Box algorithm [16], can form the basis for a single system capable of providing an integrated measurement of the structural displacements and aerodynamic loads on unsteady airfoils on a relatively large scale (wingspan on the order of $1\,\mathrm{m}$) [17]. The structural response is hereby determined by tracking fiducial markers on the surface of the wind tunnel model, while the aerodynamic loads are inferred from flow field measurements. In a recent demonstration study, this approach has been successfully used to determine the three forces in Collar's triangle acting on a flexible wing subjected to steady and unsteady inflow conditions [18].

In the present study, LPT measurements are used to characterize the aeroelastic response of a highly flexible wing in a sinusoidal gust. The design of the wing is similar to the Pazy benchmark wing that was introduced in [5], and wingtip displacements of nearly 25% of the span are observed. This study aims to extend the current state of the art in aeroelastic measurement technology by providing complete flow field measurements around the wing along the entire span, as well as structural deformation measurements, in unsteady periodic inflow conditions.

2 NON-INTRUSIVE LOAD DETERMINATION

In the approach followed in this study, the separate aeroelastic loads are derived from the integrated aeroelastic measurements using appropriate physical models. The inertial load is determined from the wing shapes that are reconstructed from the structural displacement measurements, whereas the aerodynamic load is determined from the phase-averaged flow field measurements. The elastic force is not determined explicitly in this study, it can however be derived from the other two forces based on the equilibrium of forces acting on the wing, as it is done in this study for the comparison of the non-intrusive loads with the root force measured with the force balance (see Section 4.4).

2.1 Inertial load

For the characterization of the aeroelastic interaction in response to the gust, only the dominant motion degree of freedom is considered, which is the out-of-plane deflection w of the wing in the direction perpendicular to the wing chord. A simplified one-dimensional model of the

wing with a single coordinate z along the span is therefore considered for the inertial load determination, while the other motion degrees of freedom are not taken into account.

The inertial force per unit span I' on the wing can be determined as the product of mass density and acceleration:

$$I'(z,t) = -\mu(z)\ddot{w}(z,t) \tag{1}$$

where $\mu(z)$ is the mass per unit span, and $\ddot{w}$ is the second temporal derivative of the out-of-plane wing deflection, which is calculated from the time series of reconstructed wing shapes using a second-order central finite difference scheme in this study.

2.2 Aerodynamic loads

The component of the aerodynamic force that predominantly determines the aeroelastic gust response is the lift force. Therefore, the drag force is not taken into account in this study. Following classic unsteady potential flow theory, the lift per unit span L' of an airfoil can be divided into three contributions: the lift due to bound circulation around the airfoil, the lift due to the circulation in the wake, and the lift due to added mass [19].

In the case of a relatively small degree of unsteadiness (reduced frequency $k \ll 1$) and non-zero geometrical angles of attack α, the unsteady lift response will be dominated by the lift due to bound circulation, so that the flow can be approximated as quasi-steady. In this case, the time-dependent lift per unit span $L'(t)$ is related to the bound circulation $\Gamma(t)$ through the Kutta-Zhukovsky theorem:

$$L'(t) = \rho U_\infty \Gamma(t), \tag{2}$$

where ρ is the air density and U_∞ is the freestream velocity. The value of $\Gamma(t)$ can be obtained from a measured flow velocity field $\vec{u}(t)$ with a line integral of the velocity over a path C enclosing the airfoil:

$$\Gamma(t) = -\oint_C \vec{u}(t) \cdot d\vec{s} \tag{3}$$

Previous studies on viscous flows around airfoils have shown little or no systematic dependence on the integration contour C on the determined circulation, as long as the contour is not placed in the direct vicinity of the airfoil, i.e. outside of the boundary layer [20–22]. In this study, 25 different rectangular integration contours with a distance from the airfoil between $d_{min} = 0.1c$ and $d_{min} = 0.3c$ in all four directions are used per spanwise section of the wing, as shown in Figure 1.

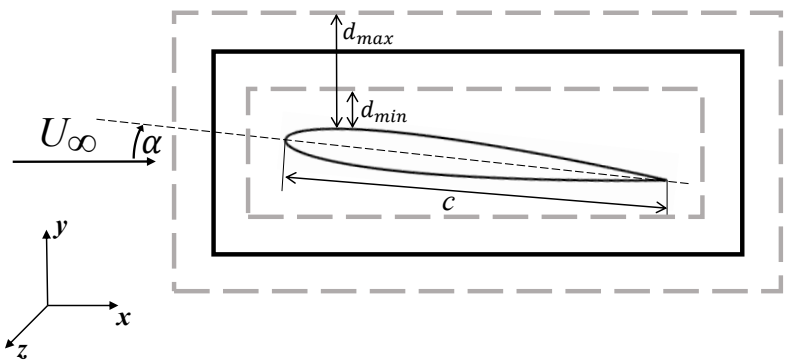

Figure 1: Sketch of a wing section with an example rectangular integration contour (black) and the limits of the range of the different contours (gray dashed)

The result from the different contours is averaged to reduce the influence of random measurement errors on the result for the lift. The effect of the circulation in the near wake downstream of the trailing edge is considered negligible in this procedure and not corrected for.

3 EXPERIMENTAL SETUP

3.1 Delft-Pazy highly flexible wing model

The experimental model in this study is nearly identical to the benchmark Pazy wing that is described in detail in [5]. The wing has a reference span of $s = 550\,\mathrm{mm}$, with a chord length of $c = 100\,\mathrm{mm}$ and a NACA 0018 airfoil section. The wing is furthermore equipped with a $300\,\mathrm{mm}$ long wingtip rod that can be be used to change the dynamic aeroelastic properties of the wing. The wing structure consists of an aluminum spar and a 3D printed nylon chassis. The assembly of the Delft-Pazy wing is performed analogously to the procedure described in [5]. The main difference to the benchmark Pazy wing design is the reduced thickness of the aluminum plate representing the spar of the Delft-Pazy wing, which is $1.5\,\mathrm{mm}$, as opposed to $2.25\,\mathrm{mm}$ for the original benchmark wing. The purpose of this design modification is to achieve similarly large deformations as observed in [5] at the reduced wind tunnel speed, which was adjusted downwards to facilitate the LPT measurements of the wing with the optical setup present in the wind tunnel test section (see Section 3.4). The mass of the wing without the base is estimated to be $300\,\mathrm{g}$, based on the information given in [5] and considering the reduced plate thickness. The skin of the Delft-Pazy wing is made of Oralight black foil with a grid of white circular markers with a diameter of $1.5\,\mathrm{mm}$ at the spanwise locations of the ribs and on the wingtip rod, to perform the measurements of the structural response of the wing in the wind tunnel. The wing geometry and the fiducial marker grid specifications are shown in Figure 2.

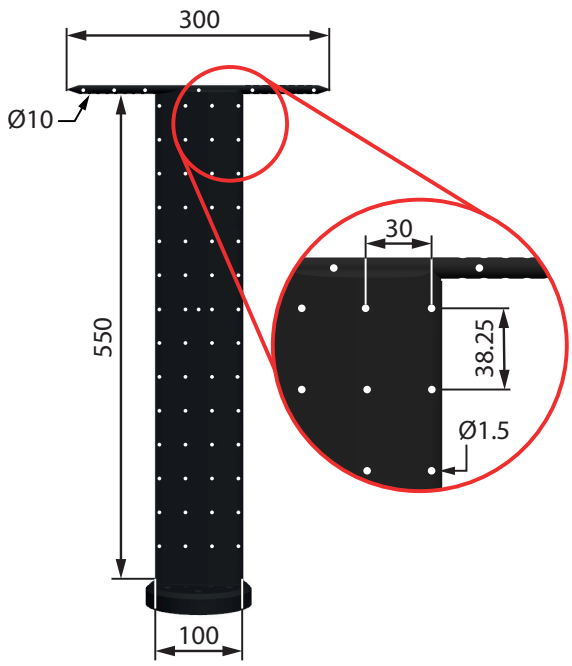

Figure 2: Sketch of the dimensions of the Delft-Pazy wing with detail of the fiducial marker grid

It should be noted that the density of the marker pattern is insufficient to directly measure the wing deformation in terms of the local strain. Instead, the purpose of the structural marker measurements is threefold; firstly, the marker measurements are used to transform the measurement coordinate system into wind tunnel coordinates as described in Section 4.1, and secondly,

they are used to determine the deformed wing shape according to the procedure described in Section 4.2, which is in turn used for the determination of the inertial force. Additionally, the marker-based wing shape is used for selecting the circulation integration contours during the aerodynamic load determination based on the flow field measurements.

3.2 Ground vibration test

A ground vibration test (GVT) of the Delft-Pazy wing was conducted to characterize its structural dynamic behavior. The GVT measurements were conducted with a Polytec PSV-500 laser scanning vibrometer in the frequency range up to 800 Hz and post-processed with SimCenter TestLab. An overview of the experimental setup of the GVT is shown in Figure 3(a). Vibration data was acquired at 37 different measurement points on the wing (see Figure 3(b)), and the data from 10 measurements were averaged for each measurement point. The excitation of the wing model was achieved with a Maul-Theet vlmpact-61 automatic modal hammer. The impact point of the modal hammer was near the leading edge of the wing at around one quarter of the wingspan measured from the base, between the third and the fourth rib, as visible in Figure 3(b). The results of the GVT in terms of the first five mode types and the modal frequencies are summarized in Table 1.

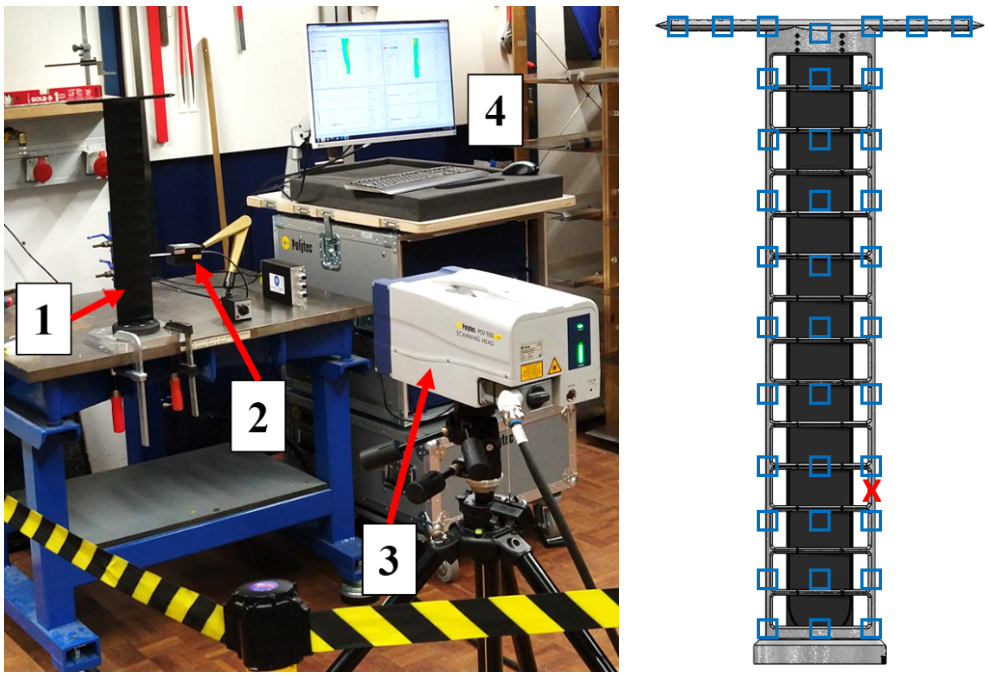

(a) (b)

Figure 3: a) Experimental setup for the ground vibration test. 1: Delft-Pazy wing, 2: modal hammer, 3: laser scanning vibrometer, 4: data acquisition computer, b) CAD model of the wing without skin, with an indication of the GVT measurement points (blue squares) and the driving point (red cross)

Table 1: Results of the ground vibration test

mode no.	mode type	modal frequency
1	first bending	3.2 Hz
2	second bending	22.5 Hz
3	first torsion	29.5 Hz
4	third bending	65.0 Hz
5	second torsion	119.7 Hz

3.3 Wind tunnel setup

The wind tunnel experiments were conducted in the Open Jet Facility (OJF) at the Delft University of Technology. The OJF is an open test section, closed-loop wind tunnel with an octagonal outlet that spans $2.85\,\mathrm{m} \times 2.85\,\mathrm{m}$, which was operated at a freestream velocity of $U_\infty = 18.3\,\mathrm{m\,s^{-1}}$ during the experiments, corresponding to a Reynolds number of $\mathrm{Re} = 122\,000$ based on the wing chord. The Delft-Pazy wing model was mounted vertically in the test section on a six-component force balance, which is attached to a rotating table that allows setting the geometric angle of attack, α, defined with respect to the steady inflow direction. The balance and the rotating table are located underneath a splitter plate to reduce wind tunnel interference effects. The wind tunnel setup with an indication of the relevant components is shown in Figure 4.

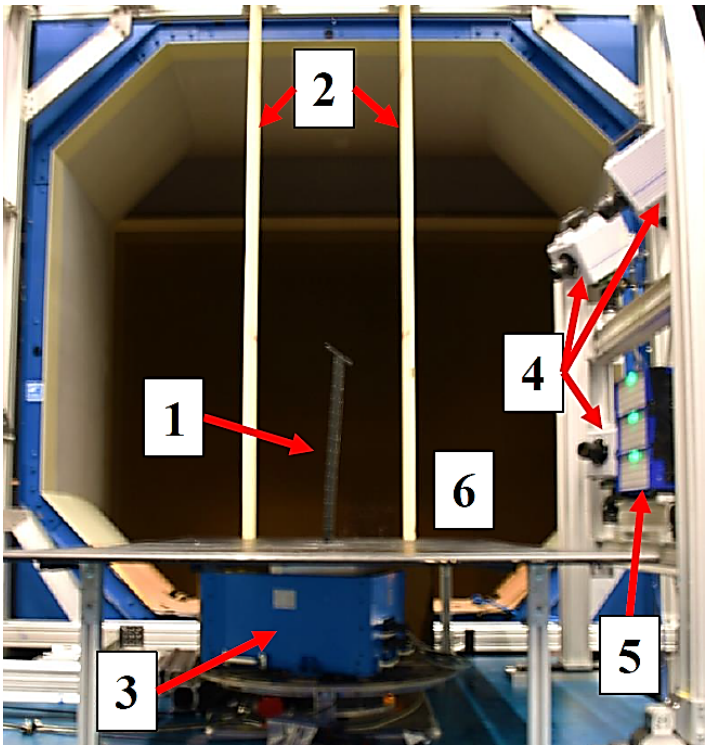

Figure 4: Photo of the wind tunnel setup in the OJF, looking upstream. 1: Delft-Pazy wing, 2: gust generator vanes, 3: six-component balance, 4: 3x high speed cameras, 5: 3x LED illumination units, 6: HFSB seeding generator, placed in the wind tunnel settling chamber (not visible in the photo)

For the experiment, a gust generator is mounted at the wind tunnel nozzle exit, which consists of two vertically mounted movable vanes that span the height of the wind tunnel nozzle [23]. Two different test cases are considered for this study, which correspond to different levels of wing deformation and degrees of unsteadiness in the periodic inflow conditions. The unsteady inflow is generated by a continuous sinusoidal operation of the gust generator during the measurement, with the gust vane angle described by $\beta = \beta_g \sin(2\pi f_g t)$, where β_g and f_g are the amplitude and frequency of the gust vane motion, respectively. The test conditions of the two test cases investigated in this study are summarized in Table 2.

Table 2: Summary of the test conditions

	geometric angle of attack α	gust vane amplitude β_g	gust frequency f_g	reduced frequency k
test case 1	$5°$	$5°$	$5.7\,\mathrm{Hz}$	0.10
test case 2	$10°$	$5°$	$3.2\,\mathrm{Hz}$	0.055

The first test case has a moderate geometric angle of attack and a gust frequency that is high enough to reach a reduced frequency $k = f\pi c U_\infty^{-1}$ that typically produces considerable unsteady aerodynamic effects [24]. The second test case has a higher geometric angle of attack, thus producing more lift, and is excited with a gust frequency that is equal to the first natural bending frequency measured in the GVT, to produce large dynamic deflections of the wing.

3.4 Lagrangian particle tracking system

For conducting the LPT measurements of the flow, the freestream is seeded with helium-filled soap bubbles (HFSB) with a diameter of about $0.5\,\mathrm{mm}$ that are used as flow tracers [25]. The HFSB seeding generator, which consists of 200 bubble-generating nozzles covering an area of approximately $0.5\,\mathrm{m}$ in width and $1\,\mathrm{m}$ in height, is placed in the settling chamber of the OJF upstream of the wind tunnel nozzle, to minimize the influence of the seeding generator on the freestream quality as well as to improve the seeding particle concentration in the test section. The working principle of the nozzles is described in [26]. The seeding particle concentration during the experiment was on the order of $1\,\mathrm{cm}^{-3}$. The optical measurement setup consists of three Photron Fastcam SA1.1 high-speed cameras that are operated at a frequency of $5.4\,\mathrm{kHz}$ with a resolution of 1 megapixel (12-bit, $20\,\mu\mathrm{m}$ pixel pitch). The illumination of the HFSB flow tracers and the fiducial markers on the wing is achieved with three LaVision LED-Flashlight 300 illumination units. The LPT data acquisition is performed with the LaVision Davis 10 software. The LPT measurement setup in the wind tunnel is shown in Figure 5.

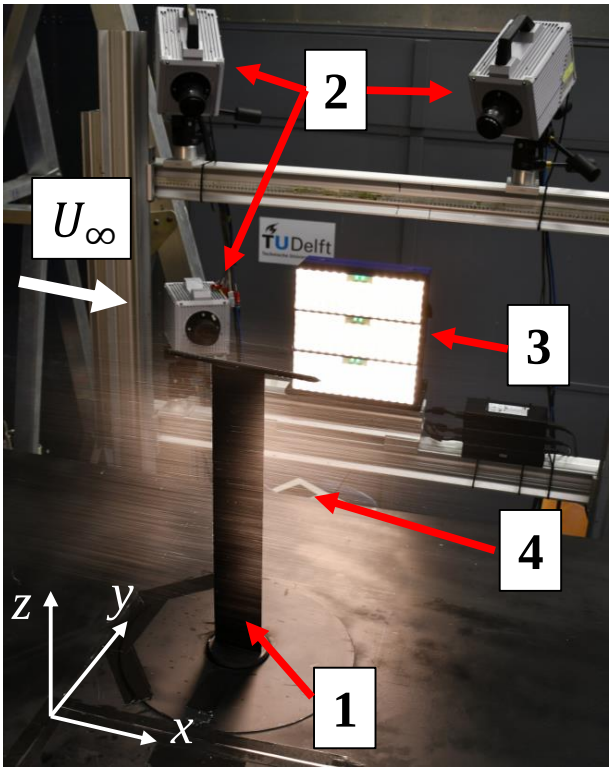

Figure 5: Photo of the Lagrangian particle tracking measurement setup in the wind tunnel. 1: Delft-Pazy wing, 2: high speed cameras, 3: LED illumination units, 4: stream of illuminated helium-filled soap bubbles

The size of the measurement volume that is obtained with this setup is about $300\,\mathrm{mm}$ in the x, y, and z directions, respectively. To achieve the complete aeroelastic characterization of the Delft-Pazy wing, which has a span width of $550\,\mathrm{mm}$, measurements of the flow field around the entire wing are necessary. Considering the measurement volume size and the limited optical access of the measurement setup, four separate measurements are performed for each test case to achieve

this, each covering one part of the entire investigated domain: one measurement on the suction and one on the pressure side for the upper and the lower half of the wingspan, respectively. For each measurement volume, five independent measurements of $1\,\mathrm{s}$ each are performed. All acquisitions from the four different measurement volumes are then combined into an integrated, phase-averaged representation during the LPT data processing. This averaging is beneficial to improve the measurement resolution, considering the limited HFSB particle concentration. The adjustment of the spanwise position of the measurement volume is performed by changing the position of the cameras and illumination with respect to the wing. In contrast, the LPT measurements on the suction and pressure side of the wing are performed without moving the optical measurement setup and instead by changing the angle of attack from a positive value of α to the corresponding negative value $-\alpha$, thereby exploiting the symmetry of the Delft-Pazy wing.

4 INTEGRATED MEASUREMENT APPROACH

The processing steps that are applied in this study to achieve the dynamic aeroelastic characterization of the periodic gust response of the Delft-Pazy wing are visualized in Figure 6. The data processing of the integrated optical measurements to obtain separate LPT measurements of the flow and the structure is described in Section 4.1. The further post-processing of these measurements to obtain the wing shape reconstruction and the phase-averaged volumetric flow fields are described in Sections 4.2 and 4.3, respectively. These results are then further processed using the physical relations described in Section 2 to achieve the aeroelastic loads on the wing in terms of the inertial loads and the lift distributions along the span in response to the periodic gust forcing, which are the key results of this study. To validate the results from the integrated measurement approach, a comparison is made to force balance measurements in terms of the root force on the wing; the procedure for this validation is described in Section 4.4.

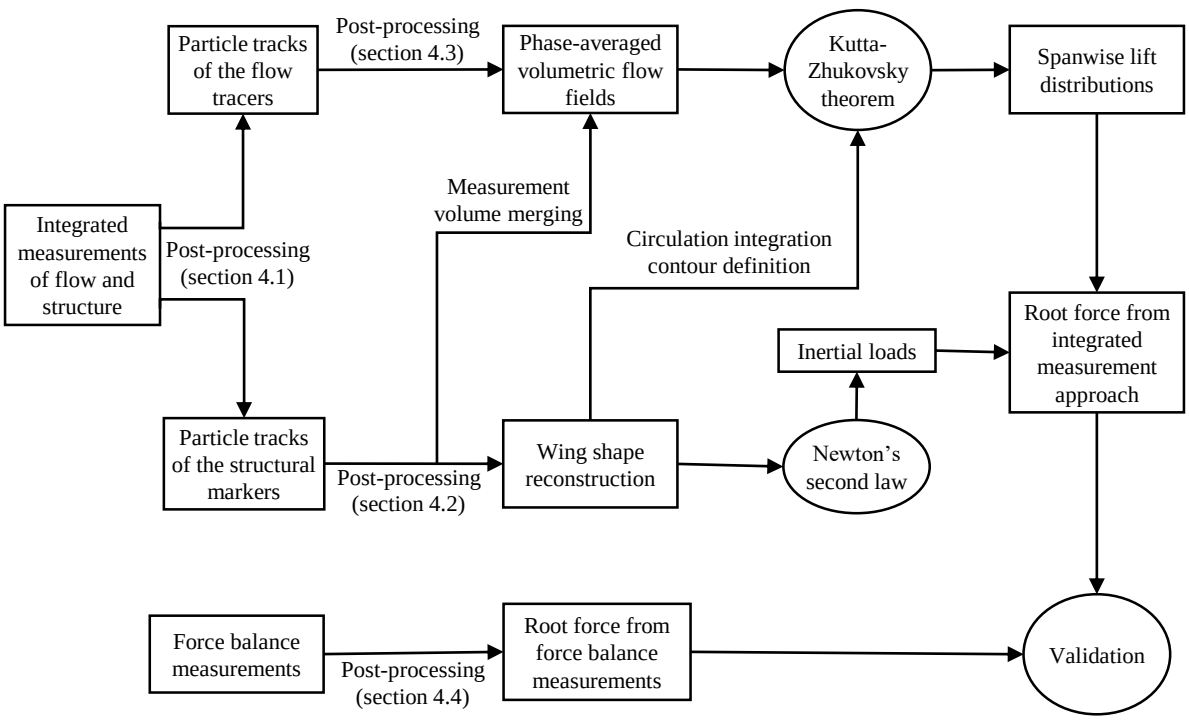

Figure 6: Flow chart of the data processing steps applied in this study

4.1 LPT data processing

The processing of the integrated optical measurements is performed with the LaVision Davis 10 software and begins with the geometrical calibration of the measurement system and a volume self-calibration [27]. Successively, the flow tracers are separated from the structural markers in the acquired images, so that a non-uniform optical transfer function [28] can be generated for the structural markers and the flow tracers separately. The removal of the structural information from the integrated measurement images is achieved with a temporal high-pass filter [29], exploiting the different time scales between the flow and the structural motion. The reverse operation is applied to obtain the image data of the structural markers without the flow tracer information, by using a temporal low-pass filter [30]. The image separation procedure is illustrated in Figure 7. After separating the flow and structural information and completing the optical calibration, the next step is to perform the LPT analysis, for which the Shake-The-Box algorithm is used [16]. The results are obtained in terms of individual Lagrangian particle tracks, with position, velocity, and acceleration of each particle over time, for both the structural markers and the flow tracers in separate data sets. These measurements are post-processed in a phase-averaged sense based on the gust excitation, as described in Sections 4.2 and 4.3.

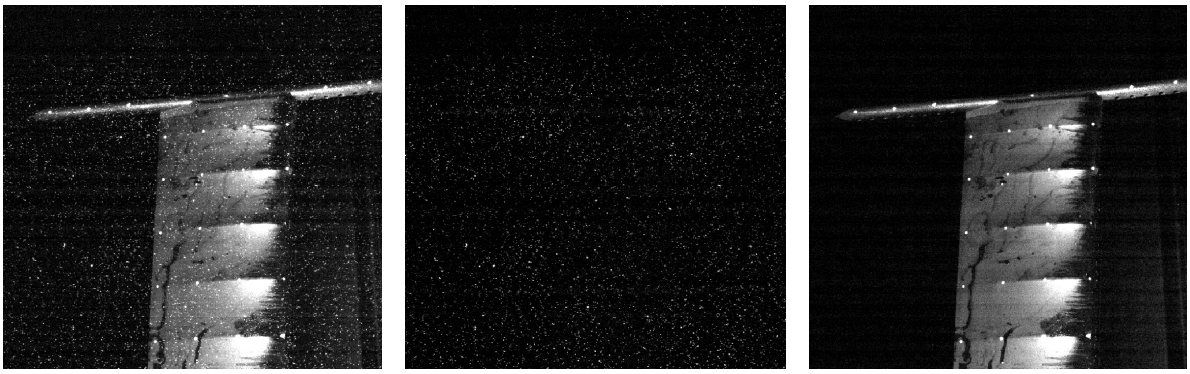

(a) (b) (c)

Figure 7: Image data processing: (a) integrated optical measurement of flow and structure, (b) image data of the flow tracers, (c) image data of the structure

A further necessary post-processing step of the LPT data is the transformation of the measurement coordinate system to the wind tunnel coordinates. This is achieved by acquiring a reference measurement of the structural markers on the wing without wind tunnel operation after each modification of the measurement volume. This data is then correlated with the reference positions of the markers painted on the model to determine the translations and rotations of the measurement coordinates with respect to the wind tunnel coordinates, which are then used to transform the LPT measurements into the wind tunnel coordinate system. The accuracy of the employed merging procedure can be assessed by comparing the measured flow velocity at corresponding positions with respect to the wing from different acquisitions. Typical values of these differences were between 1% and 3% of the local velocity magnitude. Since these values are of the same order of magnitude as when the merging of different flow measurement acquisitions is performed automatically based on position measurements with a robotic arm [31], these differences are considered acceptable and not further investigated.

4.2 Wing shape reconstruction

To reconstruct the wing shape, the marker measurements are analyzed in a phase-averaged sense, which means that measurements from different periods are collected at the respective time expressed as a fraction of the period, t/T. To reduce the effect of random measurement noise and outliers that may result from light reflections in the acquired images, a temporal smoothing procedure using a sinusoidal curve fit is applied. In the case of large wing deflections, the temporal behavior of the wing is not expected to be sinusoidal in the wind tunnel reference coordinate system, due to the rotation of the wing sections with respect to the global coordinate system. The temporal smoothing is therefore performed after transforming the marker measurements per wing section into the reference system of the static deflected wing shape at the respective angle of attack, which has been determined in a previous study [32]. When analyzed in their local reference system, the measurements of the marker position are obtained in terms of displacements normal to the static deflected position, which diminishes the effect of the wing section rotation. To ease the data processing, the marker measurements are averaged along the chord for each spanwise section where the markers were painted. This means that the twist angle of the wing ϵ is not analyzed in this study, as it was found to be relatively small ($|\epsilon| < 1°$), and its value is not directly required for the analyses performed in this study.

The displacement measurements and the corresponding curve fits are shown for both test cases in Figure 8. With the described approach, the sinusoidal curve fit provides a very good approximation of the temporal behavior, with a standard deviation of the residual of the fit on the order of $\sigma = 0.1\,\mathrm{mm}$ in test case 1 and $\sigma = 0.2\,\mathrm{mm}$ in test case 2.

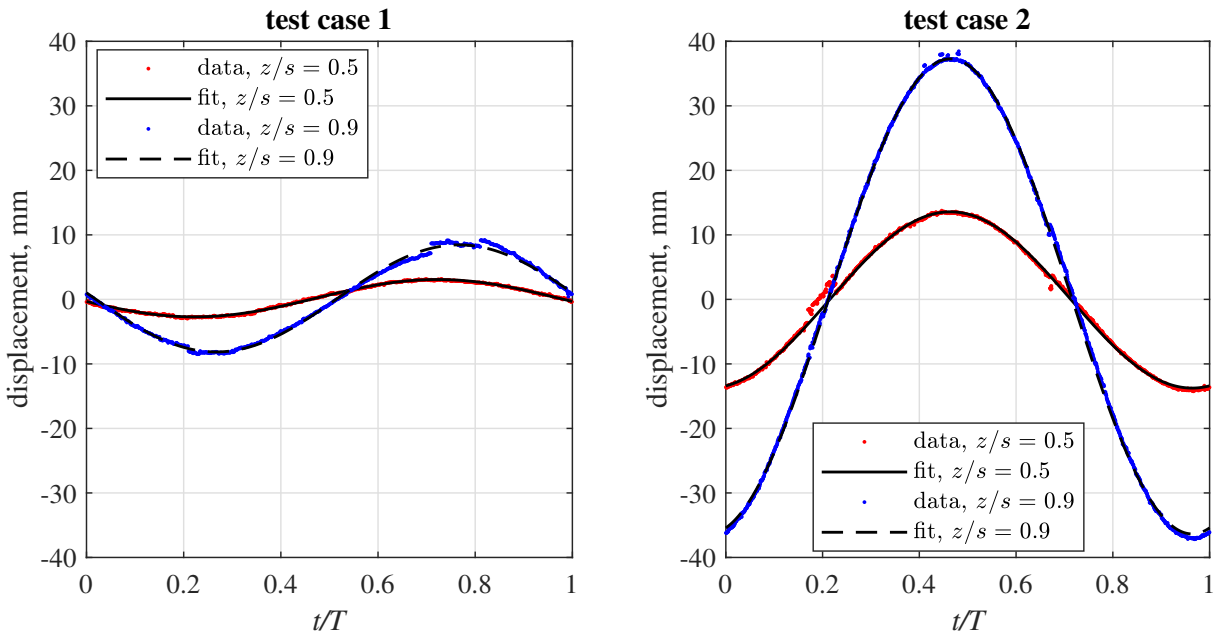

Figure 8: Displacement measurements over the period at two spanwise locations with sinusoidal fit

After the phase-averaged marker measurements per spanwise location are determined, a curve fitting procedure is applied per phase instant to yield the phase-averaged behavior of the wing deformation, where a polynomial is fitted through the measurements along the spanwise direction. Following this procedure, the polynomial curve fit can be used as a reference spanwise axis to calculate the deformed wing shape.

A fourth order polynomial is used in this study for the curve fit, which satisfies the geometric boundary conditions of a wing clamped at the root, $w(z = 0) = 0$ and $w'(z = 0) = 0$, and is defined as:

$$w(z) = Az^4 + Bz^3 + Cz^2, \tag{4}$$

where the coefficients A, B, and C are optimized to provide the best fit to the experimental measurements in a least-squares sense. The results of the polynomial curve fit to the marker measurements for both test cases at the phase instant with the maximum tip deflection are shown in Figure 9. The polynomial fit accounts for the large deflections by maintaining the arc length of the curve constant with respect to the undeformed shape, assuming that the arc length does not change during deformation. This is achieved by numerically integrating the arc length of the polynomial curve, to determine the value of z_{tip} in the deformed case.

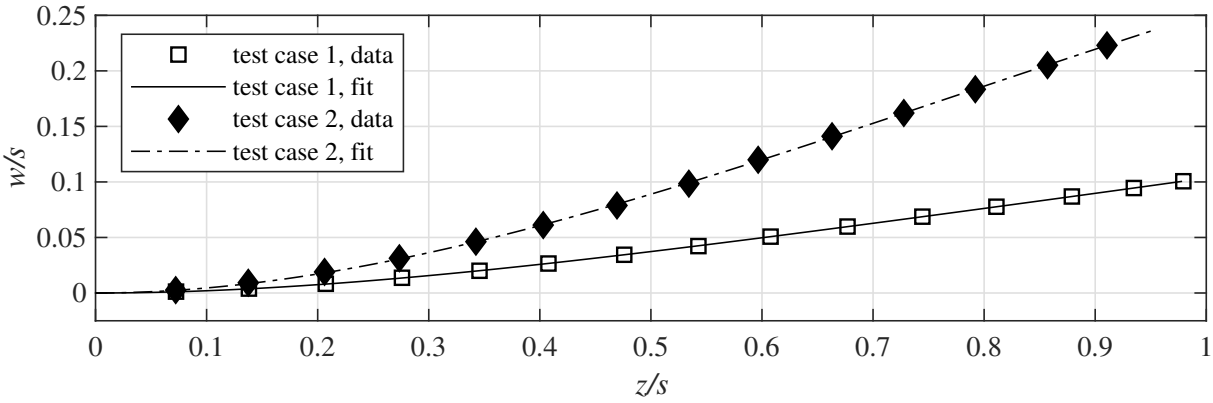

Figure 9: Wing shape measurement at maximum deflection for both test cases with polynomial curve fit

After the polynomial curve fit has been performed for all phase instants in both test cases, the obtained time series of the fitting coefficients allows the reconstruction of a smooth deformed wing shape over the entire period. These reconstructions can be directly used to compute the inertial loads along the span, and to define the circulation integration contours for the lift determination from the flow field. The main features of the dynamic gust response of the wing, determined based on the wing shape reconstruction, are summarized in Table 3.

Table 3: Summary of the dynamic gust response of the wing for both test cases

	max. tip deflection	min. tip deflection	phase shift Φ/π
test case 1	$56\,\mathrm{mm}$ $(0.103s)$	$37\,\mathrm{mm}$ $(0.067s)$	-0.97
test case 2	$133\,\mathrm{mm}$ $(0.243s)$	$43\,\mathrm{mm}$ $(0.079s)$	0.57

The dynamic response to the two different gusts is different in terms of the deflection amplitude and the phase shift Φ/π with respect to the gust arriving at the wing, despite the identical forcing amplitudes. These differences can be related to the different forcing frequencies of the gust (see Table 2) with respect to the frequencies of the dynamic modes of the Delft-Pazy wing that were identified in the GVT (see Table 1). The gust frequency of test case 1 is well above the first bending frequency of the wing, but clearly below the higher frequency modes. As a result, the dynamic response of the wing is relatively small in amplitude, with a phase shift of nearly $\Phi/\pi \approx 1$ with respect to the gust forcing. In test case 2, the frequency of the gust is identical to the frequency of the first bending mode. The dynamic response to this forcing is observed to be much larger in amplitude and shifted in phase by around $\Phi/\pi \approx 0.5$.

4.3 Flow data ensemble-averaging

The particle tracks of the flow tracers obtained from the LPT analysis provide the time series of a large number of discrete measurements of the flow velocity, obtained in the measurement coordinates of the LPT system. These measurements are then transformed into the coordinate system of the wind tunnel as described in Section 4.1 and afterward assigned a phase value t/T. Subsequently, the measurements are ensemble-averaged to a Cartesian grid as described in [33]. The ensemble-averaging is performed with 25 temporal bins along the period, each spanning a fraction of 4% of the period T. A Cartesian grid with a grid spacing of $3.75\,\mathrm{mm}$ is used, and an overlap of 75% is applied in the ensemble-averaging.

The result of the flow data post-processing is visualized in Figures 10, 11 and 12. In Figure 10, the three-dimensional reconstructed wing shape is shown in the phase instant of maximum deflection for both test cases. The ensemble-averaged flow field is visualized in four slices along the span and with two isosurfaces of the streamwise velocity. In Figures 11 and 12, the phase-averaged flow field is shown in four different phase instants for test case 1 and 2, respectively, for the spanwise location $z/s = 0.5$. The reconstructed wing position is indicated in the plots as well. The relative position of the wing section in the flow field on the Cartesian grid is used to define the circulation integration contours for the lift determination per wing section as described in Section 2.

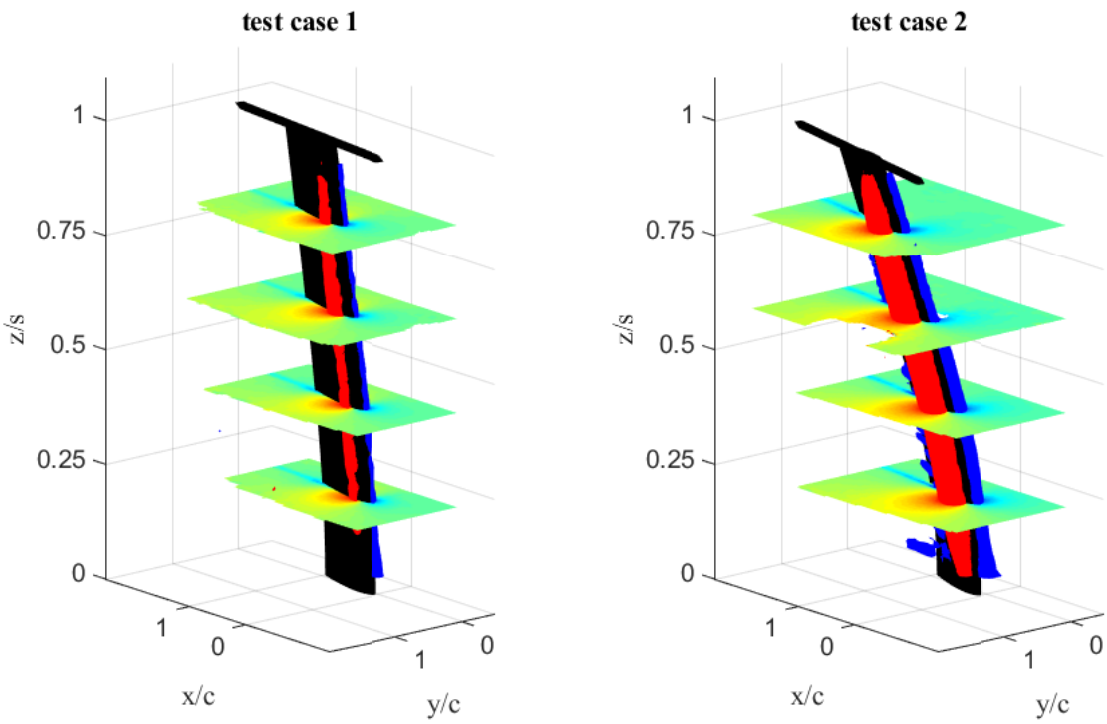

Figure 10: Marker-based wing reconstruction at the phase instant of maximum wing deflection, with isosurfaces of the ensemble-averaged streamwise velocity (blue: $0.75U_\infty$, red: $1.25U_\infty$) and four slices of the streamwise velocity field at $z/s = 0.2$, $z/s = 0.4$, $z/s = 0.6$, and $z/s = 0.8$

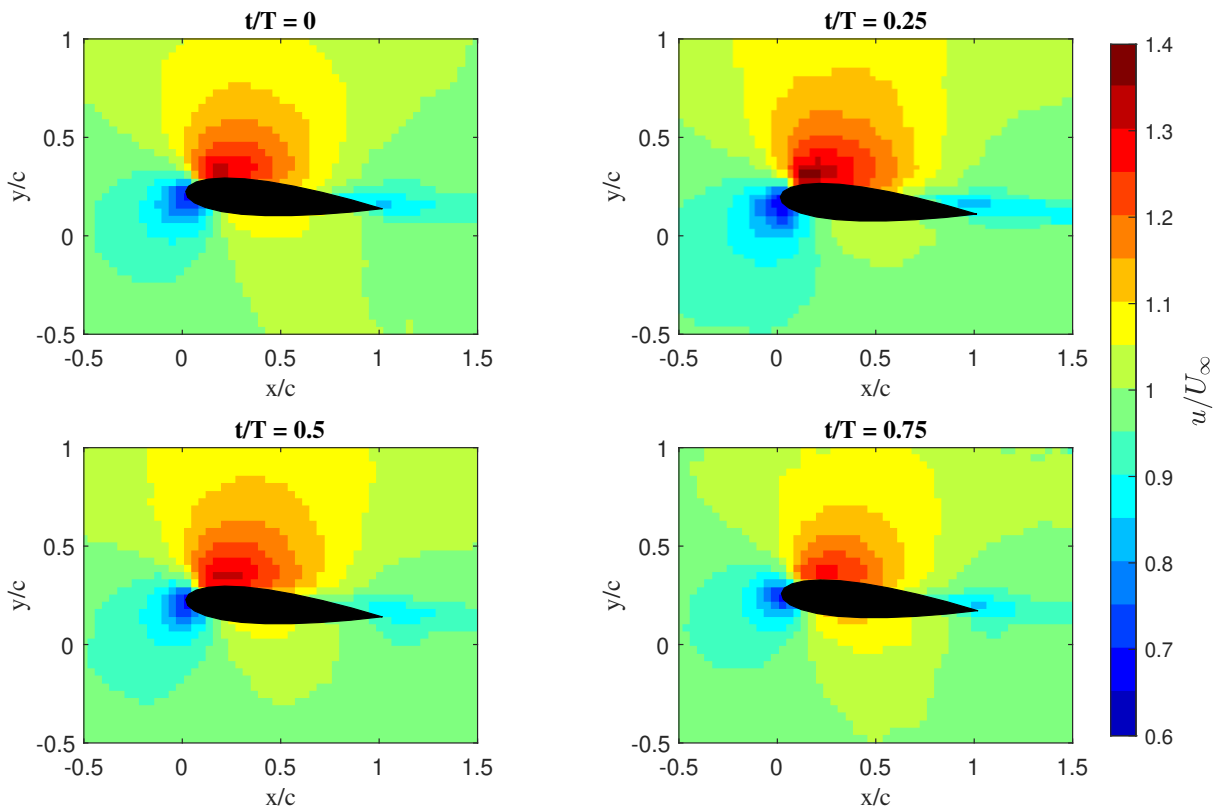

Figure 11: Ensemble-averaged streamwise velocity at mid-span in four different phase instants for test case 1

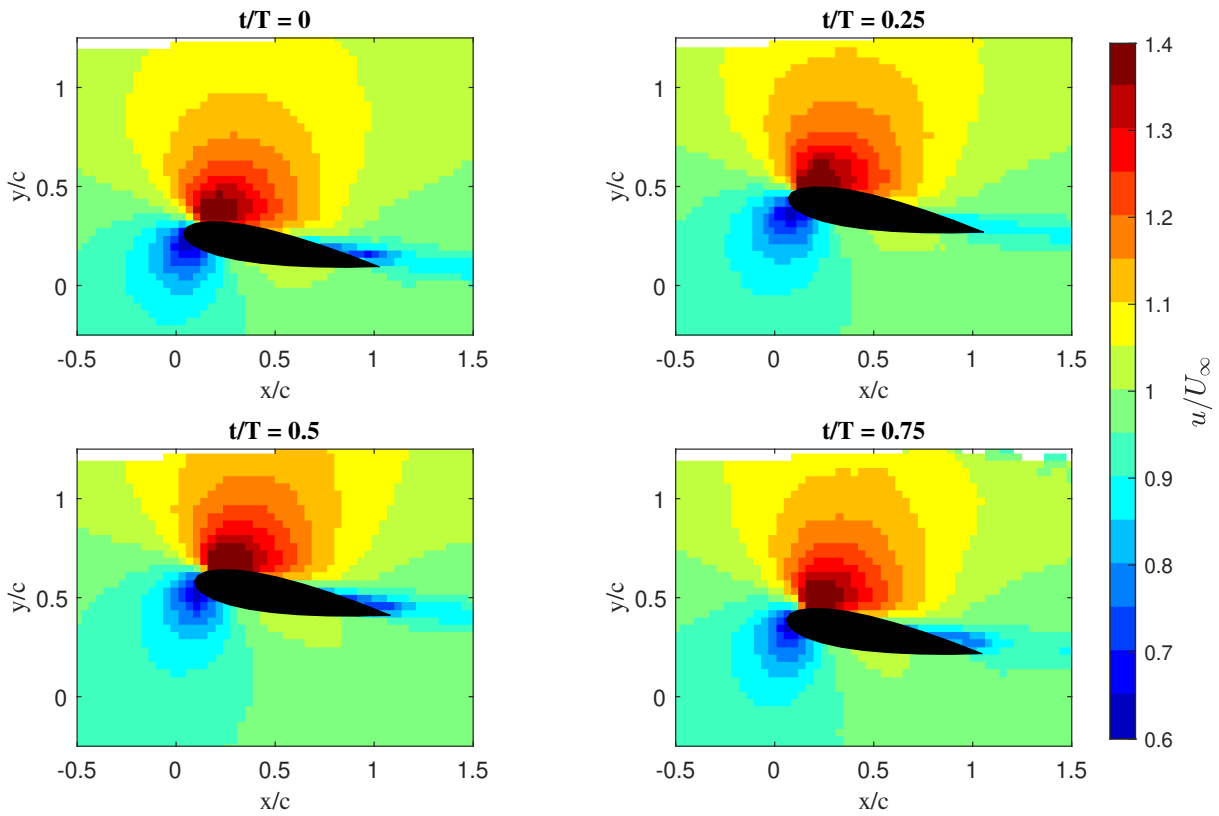

Figure 12: Ensemble-averaged streamwise velocity at mid-span in four different phase instants for test case 2

4.4 Validation with force balance measurements

The force balance data were acquired simultaneously with the optical measurements, which means that there are 20 separate measurements for each test case (five acquisitions for each of the four measurement volumes). The results for the root force in the y-direction from the force balance measurements are phase-averaged and shown in Figure 13 for both test cases.

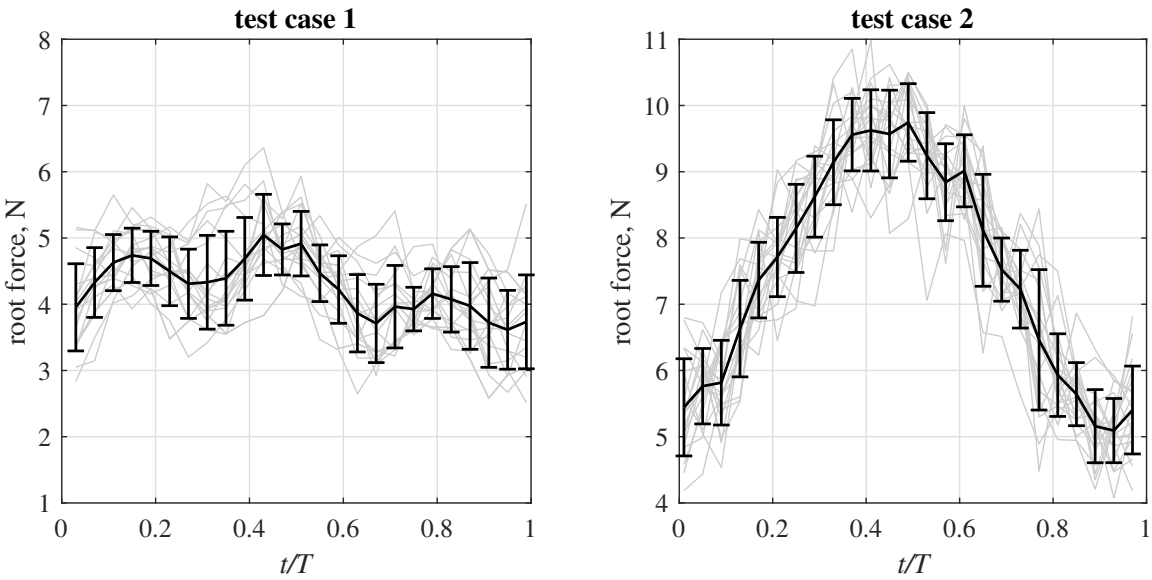

Figure 13: Balance measurements: individual acquisitions (gray), mean with standard deviation (black)

The 20 individual measurements are phase-averaged and plotted in gray in Figure 13, while the mean and the standard deviation of all measurements are depicted in black with error bars. Despite the phase-averaging of the individual measurements, the force balance data still exhibits a considerable amount of random measurement error, with standard deviations on the order of $\sigma \approx 0.6\,\mathrm{N}$ in both test cases.

To perform a validation of the aeroelastic load results obtained with the integrated measurement approach against the force balance measurements, the aerodynamic and inertial loads from the integrated approach are numerically integrated along the span.

$$\begin{aligned} F_{y,root}(t) &= \int_0^s \left(L'(z,t) + \cos\alpha I'(z,t)\right) dz \\ &= \int_0^s L'(z,t)dz - \cos\alpha \int_0^s \mu(z)\ddot{w}(z,t)dz \end{aligned} \tag{5}$$

While the lift force acts in the y-direction of the wind tunnel reference system, the inertial force was determined according to Equation 1, considering the out-of-plane deflection in the reference system of the wing, w. To obtain the integral force in the y-direction, the contribution of the inertial load is therefore reduced by a factor of $\cos\alpha$.

5 AEROELASTIC LOADS RESULTS

5.1 Inertial loads

The inertial loads as determined from the time series of the reconstructed wing shapes with the method described in Section 2 are shown in Figure 14. The results were calculated using Equation 1, based on the assumption that the mass density of the wing is constant along the span, except for the tip rod, which is taken into account as an additional tip mass. The plots show the variation of the sectional inertial force over the period at three different spanwise locations for both test cases. The temporal behavior of the inertial load is qualitatively identical for the different spanwise locations, with the load magnitude increasing with the spanwise coordinate.

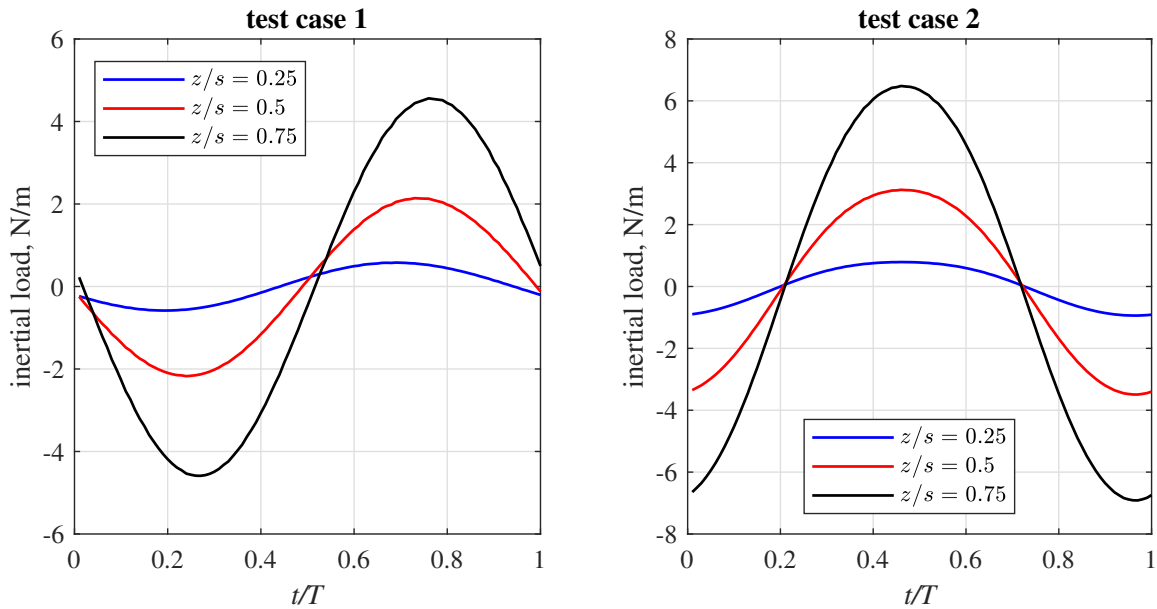

Figure 14: Sectional inertial load variation over the period at three different spanwise locations

The spanwise-integrated inertial force is shown in Figure 15 for both test cases. The magnitudes of the inertial forces are similar for both test cases, as test case 1 has a higher gust frequency while test case 2 exhibits a larger dynamic wing deflection amplitude. The phase difference between the inertial force of the two cases is around a quarter of the period as a result of the phase lag differences in the wing dynamic response (see Table 3).

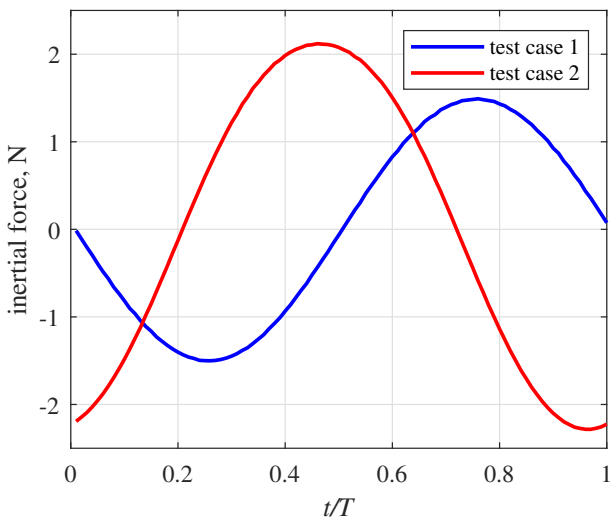

Figure 15: Inertial force variation for both test cases

5.2 Aerodynamic loads

The aerodynamic loads on the wing as determined with Equation 2 are displayed in Figures 16 and 17 in terms of the section lift coefficient, $C_\ell = L'(\frac{1}{2}\rho U_\infty^2 c)^{-1}$. In Figure 16, the spanwise lift distribution is shown at four different phase instants, while the temporal variation of the lift over the period at different spanwise locations is shown in Figure 17. The error bars in the plots indicate the standard deviation of the lift when calculating the section lift with the 25 different integration contours for obtaining the circulation as described in Section 2.

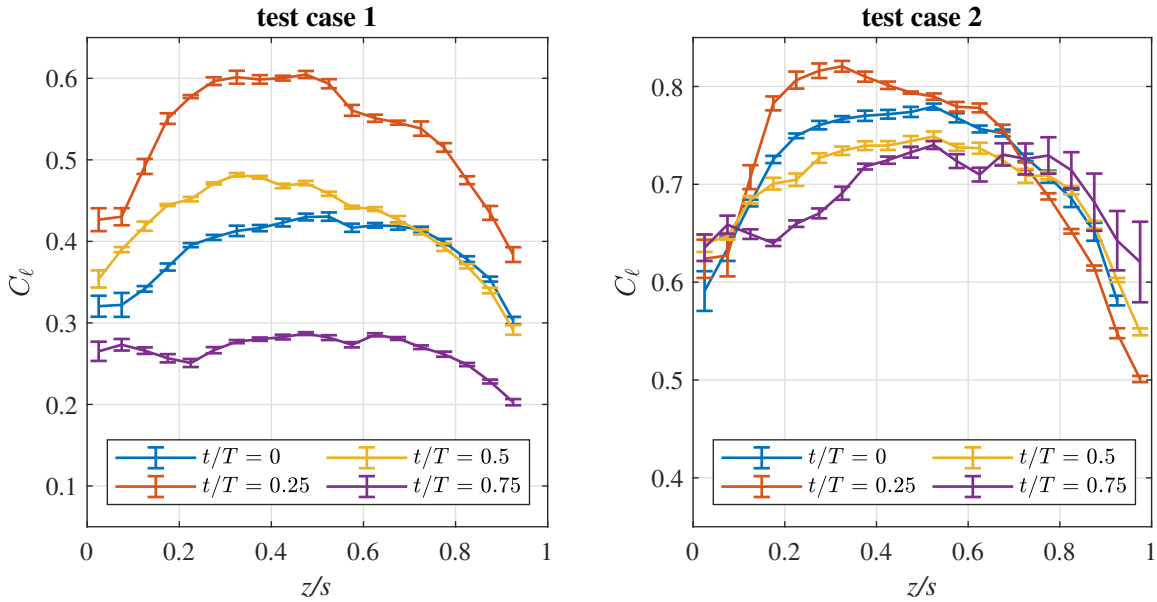

Figure 16: Sectional lift distribution along the span at four different phase instants

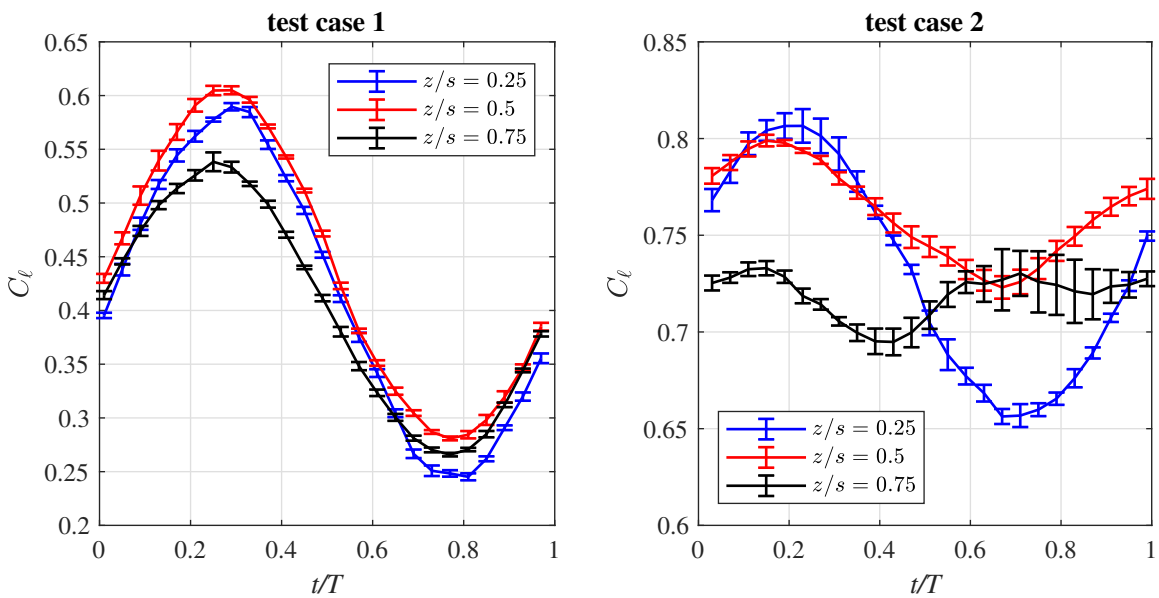

Figure 17: Sectional lift over the period at three different spanwise locations

As visible in Figure 16, the lift distributions along the span for different phase instants are qualitatively similar in test case 1 but vary in lift magnitude. This is following the sinusoidal temporal behavior of the lift for this test case that is observed in Figure 17, which only varies to a small extent in magnitude and phase for the different spanwise locations. From both figures it is evident that in this test case the maximum lift occurs near $t/T = 0.25$ over the entire wing

span. In contrast, the spanwise lift distributions in test case 2 do not vary strongly in magnitude but exhibit a qualitatively different behavior depending on the phase instant. This is reflected in the temporal behavior as well, where the lift in the lower part of the wing is still quasi-sinusoidal but shows a more complex behavior for the top part of the wing.

The temporal variation of the spanwise-integrated lift force is shown for both test cases in Figure 18. The mean value of the lift over the period is about twice as high in test case 2 when compared to test case 1, as a result of the difference in geometric angle of attack. On the other hand, the variation of the lift is considerably larger in test case 1 with a peak-to-peak amplitude of almost $3\,\mathrm{N}$, compared to less than $1\,\mathrm{N}$ in test case 2. The standard deviation of the lift variation due to the choice of the integration contour as indicated by the error bars is not significant, having typical values of less than $0.05\,\mathrm{N}$ or 1% of the mean force.

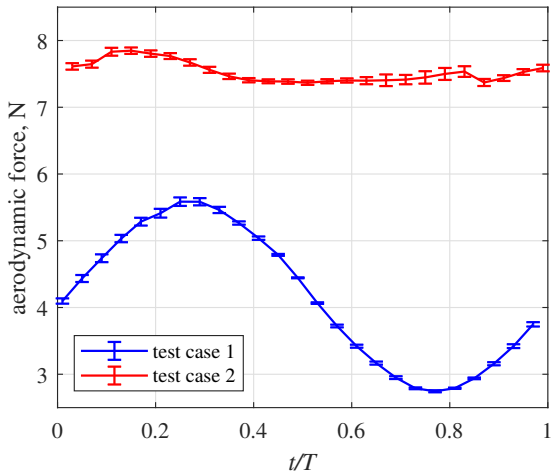

Figure 18: Aerodynamic force over the period for both test cases

5.3 Validation of the root force

The root force obtained with the integrated measurement approach as the sum of aerodynamic and inertial force according to Equation 5 is compared to the force balance measurements in Figure 19.

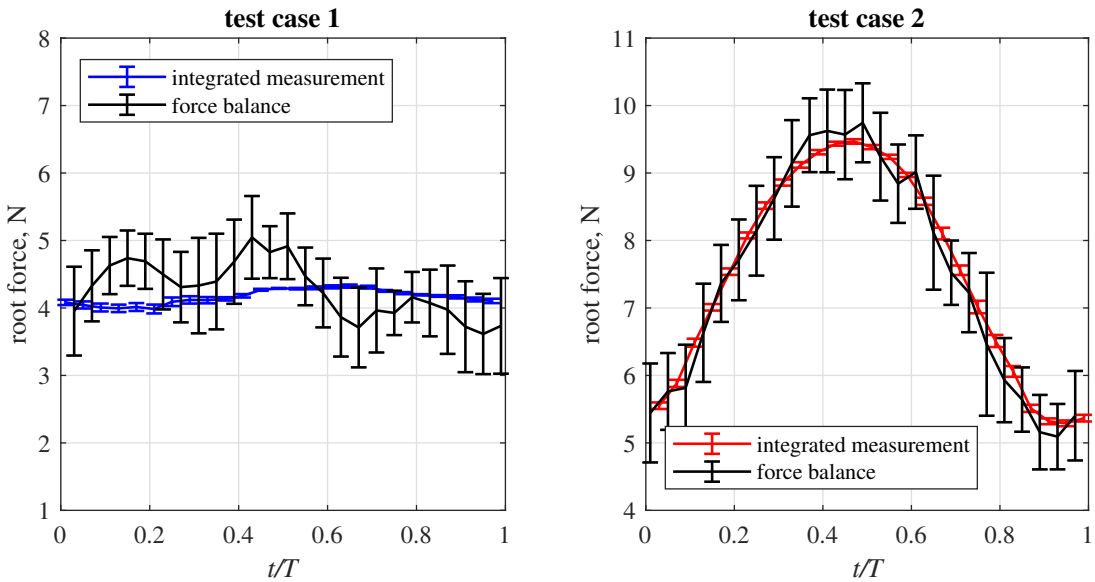

Figure 19: Comparison of the root force measured with the integrated approach and the force balance

The comparison shows a good agreement between the two methods, within the measurement uncertainty. In test case 1, the root force remains relatively constant in response to the sinusoidal gust, while an inverse $\cos$-shaped variation is observed for test case 2. When compared to the integrated measurement result, the force balance signal shows larger variations over the period, but also larger error bars than the integrated measurement result in test case 1. The root mean square of the difference between the integrated measurement and the force balance data over the period is $0.47\,\mathrm{N}$ for test case 1, which corresponds to 11.0% of $4.27\,\mathrm{N}$, which is the mean root force over the period measured with the force balance. In test case 2, the results from the different methods appear qualitatively identical, the root mean square difference between force balance and integrated measurement amounts to $0.48\,\mathrm{N}$, which corresponds to 6.3% of the mean root force $7.47\,\mathrm{N}$, as measured with the balance.

6 CONCLUSION

In this study, the dynamic aeroelastic response of a highly flexible wing to a periodic gust excitation was determined experimentally in a wind tunnel test. The wing that was investigated is the Delft-Pazy wing, an adaptation of the Pazy aeroelastic benchmark wing for lower freestream velocities. Two test cases were considered, which differed in mean angles of attack as well as excitation frequency, where one was close to the first natural bending frequency of the wing. The measurements were performed with an integrated optical system, which provides Lagrangian particle tracking measurements of the wing motion via surface marker tracking and the flow field around the wing via the tracking of helium-filled soap bubble flow tracers. These measurements were post-processed to obtain a reconstruction of the wing shape as well as the phase-averaged flow field. It was observed that the dynamic structural response in terms of deflection amplitude and phase lag to the gust forcing depends strongly on the gust frequency; the sinusoidal gust with the frequency close to the natural bending frequency of the wing produced wingtip of deflections of nearly 25% of the span, whereas the gust with a higher frequency resulted in smaller deflection amplitudes with a larger phase lag. After the post-processing of the measurements, the aerodynamic and inertial loads acting on the wing were determined through the application of physical models to the measured data. The analysis of the lift distribution on the wing during the periodic gust encounter revealed that for small wing deflections, the lift variation is sinusoidal and can thus be directly linked to the gust forcing, whereas for the test case with larger deflections, the temporal behavior of the lift varied depending on the spanwise location. The results of this analysis were compared to force balance measurements in terms of the force at the wingroot, yielding differences between 6% and 11%.

The results of the integrated measurement approach presented in this study provide insights into the aeroelastic gust response in a level of detail that is unattainable with conventional measurement approaches based on installed sensors. Particularly relevant are the measurements of the lift distribution along the entire span during the gust encounter, which have previously never been determined experimentally. The results of this study are therefore useful for the validation of aeroelastic simulation models, in particular with respect to the unsteady aerodynamic model. The use of a single measurement system for aerodynamic and structural measurements simplifies the experimental setup and data processing compared to the coordinated use of multiple measurement systems, which makes the approach presented in this study a promising method for producing experimental reference data for dynamic aeroelastic problems of different kinds in the future, such as limit-cycle oscillations. Future studies on the accuracy of the experimental approach should investigate the application of more sophisticated physical models for the load determination to improve the agreement of the results with the force balance measurements.

ACKNOWLEDGEMENT

The authors appreciate the contribution of Ariel Drachinsky and Daniella E. Raveh to this work by providing the geometry of the Pazy wing and by offering advice for the construction of the Delft-Pazy wing. Furthermore, the authors gratefully acknowledge the help of Adrián Grille Guerra during the wind tunnel experiment. This work has been carried out in the context of the HOMER (Holistic Optical Metrology for Aero-Elastic Research) project that has received funding from the European Union's Horizon 2020 research and innovation programme under grant agreement No 769237.

7 REFERENCES

[1] Dimitriadis, G. (2017). *Introduction to Nonlinear Aeroelasticity*. Wiley & Sons.

[2] Bernhammer, L. O., de Breuker, R., and Karpel, M. (2017). Geometrically nonlinear structural modal analysis using fictitious masses. *AIAA Journal*, 55(10), 3584–3593.

[3] Kantor, E., Raveh, D. E., and Cavallaro, R. (2019). Nonlinear structural, nonlinear aerodynamic model for static aeroelastic problems. *AIAA Journal*, 57(5), 2158–2170.

[4] Drachinsky, A. and Raveh, D. E. (2020). Modal rotations: A modal-based method for large structural deformations of slender bodies. *AIAA Journal*, 58(7), 3159–3173.

[5] Avin, O., Raveh, D. E., Drachinsky, A., et al. (2022). Experimental aeroelastic benchmark of a very flexible wing. *AIAA Journal*, 60(3), 1745–1768.

[6] Collar, A. R. (1946). The expanding domain of aeroelasticity. *The Aeronautical Journal*, 50(428), 613–636.

[7] Tang, D. and Dowell, E. H. (2016). Experimental aeroelastic models design and wind tunnel testing for correlation with new theory. *Aerospace*, 3(2).

[8] Liu, T., Burner, A. W., Jones, T. W., et al. (2012). Photogrammetric techniques for aerospace applications. *Progress in Aerospace Sciences*, 54, 1–58.

[9] Raffel, M., Willert, C. E., Scarano, F., et al. (2018). *Particle Image Velocimetry: A Practical Guide*. Springer.

[10] Gherlone, M., Cerracchio, P., and Mattone, M. (2018). Shape sensing methods: Review and experimental comparison on a wing-shaped plate. *Progress in Aerospace Sciences*, 99, 14–26.

[11] van Oudheusden, B. W. (2013). PIV-based pressure measurement. *Measurement Science and Technology*, 24(3), 032001.

[12] Rival, D. E. and van Oudheusden, B. W. (2017). Load-estimation techniques for unsteady incompressible flows. *Experiments in Fluids*, 58(3), 1–11.

[13] Liu, T., Montefort, J., Gregory, J., et al. (2011). Wing deformation measurements from pressure sensitive paint images using videogrammetry. In *41st AIAA fluid dynamics conference and exhibit*. p. 3725.

[14] Marimon Giovannetti, L., Banks, J., Turnock, S. R., et al. (2017). Uncertainty assessment of coupled digital image correlation and particle image velocimetry for fluid-structure interaction wind tunnel experiments. *Journal of Fluids and Structures*, 68, 125–140.

[15] Zhang, P., Peterson, S. D., and Porfiri, M. (2019). Combined particle image velocimetry/digital image correlation for load estimation. *Experimental Thermal and Fluid Science*, 100, 207–221.

[16] Schanz, D., Gesemann, S., and Schröder, A. (2016). Shake-the-box: Lagrangian particle tracking at high particle image densities. *Experiments in fluids*, 57(5), 1–27.

[17] Mertens, C., Sciacchitano, A., van Oudheusden, B. W., et al. (2021). An integrated measurement approach for the determination of the aerodynamic loads and structural motion for unsteady airfoils. *Journal of Fluids and Structures*, 103, 103293.

[18] Mertens, C., de Rojas Cordero, T., Sodja, J., et al. (2022). Aeroelastic characterization of a flexible wing using particle tracking velocimetry measurements. *AIAA Journal*, 60(1), 276–286.

[19] Theodorsen, T. (1949). General theory of aerodynamic instability and the mechanism of flutter. Tech. Rep. TR-496, NACA.

[20] Mertens, C., Costa Fernández, J. L., Sciacchitano, A., et al. (2021). Gridless determination of aerodynamic loads using lagrangian particle tracks. In *14th International Symposium on Particle Image Velocimetry*.

[21] Sharma, S. D. and Deshpande, P. J. (2012). Kutta–Joukowsky theorem in viscous and unsteady flow. *Experiments in fluids*, 52(6), 1581–1591.

[22] Olasek, K. and Karczewski, M. (2021). Velocity data-based determination of airfoil characteristics with circulation and fluid momentum change methods, including a control surface size independence test. *Experiments in Fluids*, 62(5), 1–21.

[23] Lancelot, P. M. G. J., Sodja, J., Werter, N. P. M., et al. (2017). Design and testing of a low subsonic wind tunnel gust generator. *Advances in aircraft and spacecraft science*, 4(2), 125.

[24] Leishman, G. J. (2006). *Principles of helicopter aerodynamics*. Cambridge University Press.

[25] Scarano, F., Ghaemi, S., Caridi, G. C. A., et al. (2015). On the use of helium-filled soap bubbles for large-scale tomographic PIV in wind tunnel experiments. *Experiments in Fluids*, 56(2), 1–12.

[26] Faleiros, D. E., Tuinstra, M., Sciacchitano, A., et al. (2019). Generation and control of helium-filled soap bubbles for PIV. *Experiments in Fluids*, 60(3), 1–17.

[27] Wieneke, B. (2008). Volume self-calibration for 3D particle image velocimetry. *Experiments in fluids*, 45(4), 549–556.

[28] Schanz, D., Gesemann, S., Schröder, A., et al. (2012). Non-uniform optical transfer functions in particle imaging: calibration and application to tomographic reconstruction. *Measurement Science and Technology*, 24(2), 024009.

[29] Sciacchitano, A. and Scarano, F. (2014). Elimination of PIV light reflections via a temporal high pass filter. *Measurement Science and Technology*, 25(8), 084009.

[30] Mitrotta, F. M., Sodja, J., and Sciacchitano, A. (2022). On the combined flow and structural measurements via robotic volumetric PTV. *Measurement Science and Technology*, 33(4), 045201.

[31] Jux, C., Sciacchitano, A., Schneiders, J. F., et al. (2018). Robotic volumetric PIV of a full-scale cyclist. *Experiments in Fluids*, 59(4), 1–15.

[32] Mertens, C., Sodja, J., Sciacchitano, A., et al. (2022). Experimental aeroelastic characterization of a very flexible wing in steady and unsteady inflow. In *AIAA SciTech 2022 Forum*.

[33] Agüera, N., Cafiero, G., Astarita, T., et al. (2016). Ensemble 3D PTV for high resolution turbulent statistics. *Measurement Science and Technology*, 27(12), 124011.

COPYRIGHT STATEMENT

The authors confirm that they, and/or their company or organization, hold copyright on all of the original material included in this paper. The authors also confirm that they have obtained permission, from the copyright holder of any third party material included in this paper, to publish it as part of their paper. The authors confirm that they give permission, or have obtained permission from the copyright holder of this paper, for the publication and distribution of this paper as part of the IFASD-2022 proceedings or as individual off-prints from the proceedings.